



Title	Spherical shell structure of distribution of images reconstructed by diffractive imaging
Author(s)	Shioya, Hiroyuki; Maehara, Yosuke; Gohara, Kazutoshi
Citation	Journal of the Optical Society of America A, 27(5), 1214-1218 https://doi.org/10.1364/JOSAA.27.001214
Issue Date	2010-05
Doc URL	http://hdl.handle.net/2115/45416
Rights	© 2010 Optical Society of America, Inc.
Type	article
File Information	20100501Shioya_Maehara_Gohara_J.Opt.Soc.Am.A.pdf



[Instructions for use](#)

Spherical shell structure of distribution of images reconstructed by diffractive imaging

Hiroyuki Shioya,^{1,*} Yosuke Maehara,² and Kazutoshi Gohara²

¹*Division of Information and Electronic Engineering, Muroran Institute of Technology,
27-1 Mizumoto, Muroran 050-8585, Japan*

²*Division of Applied Physics, Graduate School of Engineering, Hokkaido University,
N13, W8, Kita-ku, Sapporo 060-8628, Japan*

*Corresponding author: shioya@csse.muroran-it.ac.jp

Received January 14, 2010; revised February 26, 2010; accepted March 5, 2010;
posted March 23, 2010 (Doc. ID 122473); published April 30, 2010

Image reconstruction from Fourier intensity through phase retrieval was investigated when the intensity was contaminated with Poisson noise. Although different initial conditions and/or the instability of the iterative phase retrieval process led to different reconstructed images, we found that the distribution of the resulting images in both the object and Fourier spaces formed spherical shell structures. Averaging of the images over the distribution corresponds to the position of the image at the sphere center. © 2010 Optical Society of America

OCIS codes: 100.5070, 100.3008.

1. INTRODUCTION

General scattering experiments give us only the scattered intensity without phase information. Since a scattered field with amplitude and phase information is a Fourier transform of the scatterer density, the use of an inverse Fourier transform, for example, by using lenses in visible optics, allows us to reconstruct the image of the scatterers. However, when ideal lenses are not available as probes in a scattering experiment, phase retrieval from the intensity is essential to reconstruct the object density. The possibility of phase retrieval was first pointed out by Sayre [1] in terms of Shannon's sampling theorem. An iterative algorithm with the Fourier transform for phase retrieval was presented by Gerchberg and Saxton [2]. Fienup presented an error reduction (ER) algorithm based on the steepest-descent method and the hybrid input-output (HIO) algorithm [3]. Phase retrieval with these algorithms has been widely used in various fields including astronomy, general optics, x-ray crystallography, and electron microscopy. A good explanation of why phases can be retrieved from the oversampled diffraction intensities is introduced in [4]. After the first report of lensless imaging in a soft x-ray region by Miao *et al.* [5], this field—often called diffractive imaging [6]—has expanded rapidly by using various probes such as x-rays [7–10], electrons [11–14], and the higher harmonics of tabletop lasers [15].

The theoretical and empirical analyses of phase retrieval have contributed to obtain most plausible images from diffraction patterns with respect to both domain constraints [16,17]. As a remarkable method for phase retrieval, averaging methods using phase-retrieved images were presented by Miao *et al.* [18], Chapman *et al.* [19], and Thibault *et al.* [20]. Such methods have been empirically used to obtain feasible images from diffraction patterns. Two kinds of averaging methods for phase retrieval

have been proposed for an advanced usage. One is the use of different runs of phase retrieval by [18,19] and the other is the average of various images obtained in the final process of iterative phase retrieval [20]. These methods differ in the preparation of prior images fitting the given noisy Fourier intensity. However, the grounds for averaging the estimated images are not yet clear. Making up this lack of clarity is important to establish this usage as a confident algorithm for imaging. More concretely, we focus on the structure of a distribution of the estimated images in the object space and the relationship between these images and their average.

In this paper, the spherical shell structures of a distribution consisting of phase-retrieved images are found from the Poisson-noise-contaminated Fourier intensity through numerical examples. The spherical structure gives theoretical support to the use of an average image by [18–20].

2. PHASE RETRIEVAL

The retrieval of the Fourier phase using intensity measurements was first presented in the cyclic transform of the Gerchberg–Saxton iterative algorithm shown in Fig. 1 [2]. The previous object ρ is transformed into F by the Fourier transform \mathcal{F} ; F is replaced with F' (the amplitude is given by the experiment in the Fourier domain, and the phase of F' is the same as that of F , while the replaced amplitude is the constraint in the Fourier domain); ρ' is obtained by the inverse Fourier transform \mathcal{F}^{-1} of F' ; and ρ' is replaced with the updated object as the next ρ using some constraints in the object domain. The object domain X is defined as a discrete squared array, and the Fourier domain K is also defined as the same as domain X with the discrete Fourier transform for practical computation.

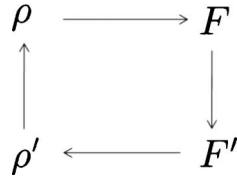


Fig. 1. Gerchberg-Saxton iterative diagram for phase retrieval.

In the following, the terminologies of *object* and *domain* are referred to interchangeably as *image* and *space*.

In the mathematical treatment of phase retrieval, let S_{obj} be the set of objects satisfying the object-domain constraints and S_{obs} be the set of objects satisfying the Fourier-domain constraint $|F_{\text{obs}}|^2$. However, there are certain kinds of obstacle factors in the measured $|F_{\text{obs}}|$ —e.g., Poisson noise and the lack of intensity caused by the direct beam—that make it difficult to estimate the missing Fourier phase. Thus an implausible object influenced by such factors could be derived with an iterative phase-retrieval algorithm. The most plausible object, ρ_{obj} , is presented as a pair given by minimizing the distance between elements of S_{obj} and S_{obs} as

$$(\rho_{\text{obs}}, \rho_{\text{obj}}) = \arg \min_{\rho_1 \in S_{\text{obs}}, \rho_2 \in S_{\text{obj}}} L(\rho_1, \rho_2), \quad (1)$$

where $\rho_{\text{obs}} \in S_{\text{obs}}$, $\rho_{\text{obj}} \in S_{\text{obj}}$, and $L(\rho_1, \rho_2) = \sum_{\mathbf{r} \in X} |\rho_1(\mathbf{r}) - \rho_2(\mathbf{r})|$. If $S_{\text{obj}} \cap S_{\text{obs}} \neq \phi$, there exists a target element ρ_{obj} satisfying $\rho_{\text{obs}} = \rho_{\text{obj}}$. Otherwise, in the case of $S_{\text{obj}} \cap S_{\text{obs}} = \phi$, ρ_{obj} in Eq. (1) is an estimated object not satisfying the Fourier-domain constraint.

The iterative phase-retrieval algorithm by Gerchberg and Saxton [2] is regarded as a method of establishing minimization with an update from the n th object ρ_n to the $(n+1)$ th object ρ_{n+1} as

$$\rho_{n+1}(\mathbf{r}) = \begin{cases} \rho'_n(\mathbf{r}), & \mathbf{r} \notin D \\ 0, & \mathbf{r} \in D \end{cases}, \quad (2)$$

where D is the set of points at which ρ'_n violates the object-domain constraints. Based on the minimization in Eq. (1), ρ'_n and ρ_{n+1} are in S_{obs} and S_{obj} , respectively, and for a sufficiently small difference between ρ'_n and ρ_{n+1} , an estimate of the object is given by ρ_{n+1} .

In the initial state of the phase-retrieval process, a prior object is very far from the plausible object; hence, the HIO algorithm is often used as an improved version of

the updating method with respect to the region violating the object-domain constraints [3],

$$\rho_{n+1}(\mathbf{r}) = \begin{cases} \rho'_n(\mathbf{r}), & \mathbf{r} \notin D \\ \rho_n(\mathbf{r}) - \beta \rho'_n(\mathbf{r}), & \mathbf{r} \in D \end{cases}, \quad (3)$$

where β is a positive constant. The HIO provides a typical change to the object ρ'_n on the set of points not satisfying the object-domain constraints. Both of these algorithms have been used connectively, and a charge-flipping algorithm was recently introduced with a different object-domain constraint [16].

3. STRUCTURE OF DISTRIBUTION OF PHASE-RETRIEVED IMAGES

The following is an example of our numerical simulations to investigate the structures of phase-retrieved images. We chose a two-dimensional figure ρ_{org} as the original image on a discrete square array domain X (256×256) shown in Fig. 2(a). F_{org} is the Fourier transform of ρ_{org} . The observed Fourier intensity including Poisson noise is regarded as a random sample from the Poisson distribution with the intensity $I_{\text{org}} = |F_{\text{org}}|^2$ as the expectation. Following Choi and Lanterman [17], the Poisson-noise-contaminated intensity for each element \mathbf{k} in the Fourier domain K is obtained by

$$\text{Poisson}\{cI_{\text{org}}(\mathbf{k})\} \sim I_{\text{noise}}(\mathbf{k}), \quad (4)$$

where the coefficient c is 3.332×10^{-9} based on $c = (\text{total count}) / \sum_{\mathbf{k} \in K} I_{\text{org}}(\mathbf{k})$ and the total count is settled by 2×10^4 , and where “ \sim ” means that the right part of the equation is a random sample from the probability distribution of the left part. Figures 2(b) and 2(c) are the Fourier intensity I_{org} ($=|F_{\text{org}}|^2$) and the Poisson noise intensity I_{noise} ($=|F_{\text{poisson}}|^2$) due to Eq. (4) with the logarithmic scale, respectively. A sufficient support area is given as one of the object-domain constraints. The objective is to find the image that best fits the original one using the Fourier intensity I_{noise} contaminated by Poisson noise.

Using 10,000 different initial images, 10,000 kinds of the estimated images (ρ_1, \dots, ρ_M , with $M=10,000$) are obtained with the HIO (1000 iterations) and the ER (2000 iterations). Figures 3(a)–3(c) are three examples of these estimated images. Although they closely resemble each other at the first glance, their structures differ upon

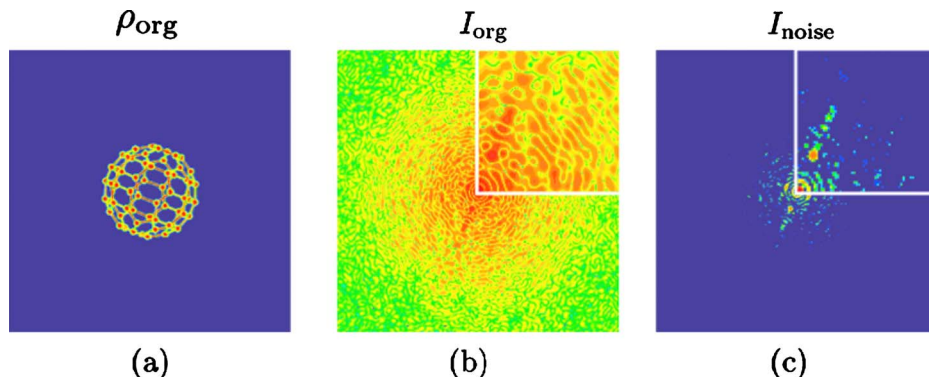


Fig. 2. (Color online) (a) ρ_{org} used as the original image. (b) Fourier intensity I_{org} obtained by Fourier transform of ρ_{org} . (c) Poisson-noise-contaminated intensity I_{noise} obtained from Eq. (4). The insets in (b) and (c) are each an enlargement of a quarter.

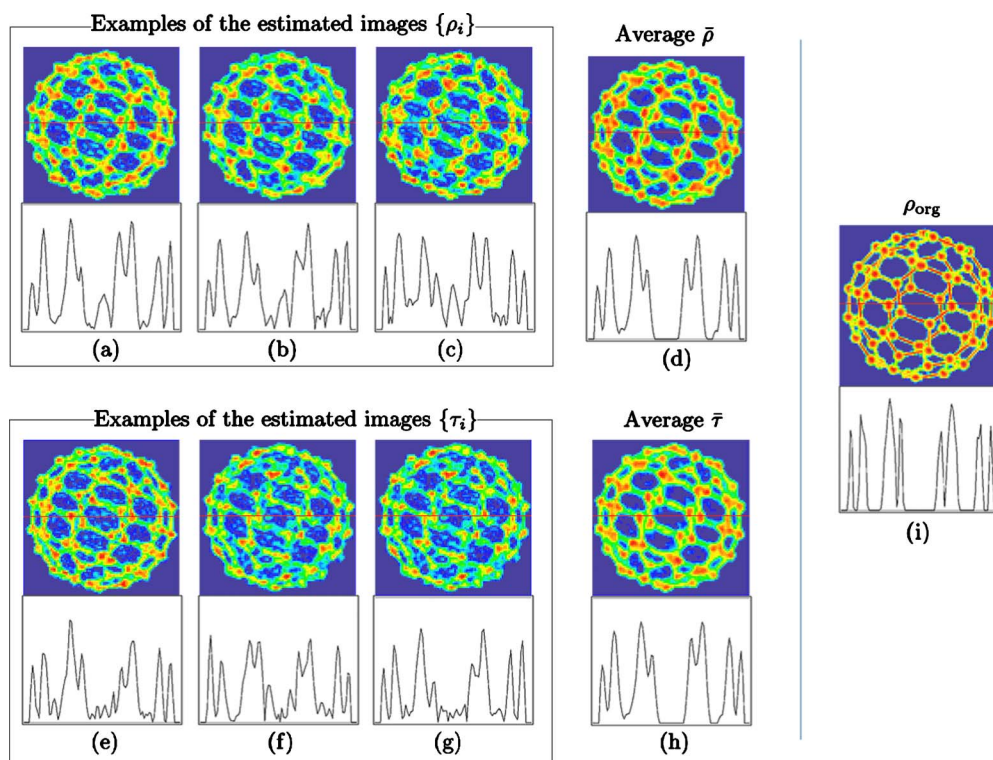


Fig. 3. (Color online) (a)–(c) Three examples of estimated images ρ_i ($i=1,2,3$) using three different initial conditions. The noise-contaminated-diffraction pattern in Fig. 2(c) was used for the diffractive imaging. (d) Average image $\bar{\rho}$ taken from the average of 10,000 estimated images $\{\rho_1, \dots, \rho_{10,000}\}$. (e)–(g) Three examples of estimated images τ_i ($i=1,2,3$) chosen during the final stage of iterations. Figure 2(c) was also used for the diffractive imaging. (h) Average image $\bar{\tau}$ taken from the average of 10,000 estimated images $\{\tau_1, \dots, \tau_{10,000}\}$. (i) Original image ρ_{org} . A line profile along each thin solid horizontal red line is shown just under each image.

closer inspection. Figures 3(d) and 3(i) are the average image $\bar{\rho}$ ($=\sum_{i=1}^M \rho_i/M$) and the original image ρ_{org} , respectively. The profile under each image is a line profile marked by a horizontal line. The average image $\bar{\rho}$ and ρ_{org} resemble each other. The zero intensity region of the profile in Fig. 3(d) shows good agreement with the corresponding region in Fig. 3(i). However, no such regions are found in the profiles of Figs. 3(a)–3(c) due to the influence of noise.

To calculate different reconstructions during one run of the algorithm, a single phase retrieval with the HIO (1000 iterations) proceeds, and 10,000 different estimated images (τ_1, \dots, τ_M , with $M=10,000$) are generated after each of 10,000 recitations of 50 HIO and 150 ER iterations. Figures 3(e)–3(g) are three examples of these estimated images. Although they closely resemble each other at the first glance, their structures differ upon closer inspection. Figure 3(h) is the average image $\bar{\tau}$ ($=\sum_{i=1}^M \tau_i/M$). The profile under each image is a line profile marked by a horizontal line. The image and its profile of $\bar{\tau}$ in Fig. 3(h) show good agreement with those of $\bar{\rho}$ in Fig. 3(d). The noise intensities are found in the regions of profiles in Figs. 3(e)–3(g) corresponding to the zero intensity region of the profile in Fig. 3(h).

Although the shapes of the estimated images are distinct in each method, their R -factors are almost the same. Therefore, it is not appropriate to estimate any of the fine characteristics by using only one estimation method. The profiles clearly show that two average images [Figs. 3(d) and 3(h)] are close to the original image ρ_{org} , whereas

each estimated image is not. This means that an averaging method is feasible for phase retrieval when the Poisson noise contaminates the Fourier intensity.

To assess the validity of the averaging of estimated images, we investigate the distributions of the individual images (ρ_i 's or τ_i 's) that are used to calculate the average image. Let X and K be the object and Fourier spaces; we use a distance L to represent the difference between two images or these Fourier transformations.

We formalize the subset of $\{\rho_1, \dots, \rho_M\}$ in order to satisfy the constraint of the distance L from the average image $\bar{\rho}$ as

$$A_\rho = \{\rho_i | L(\bar{\rho}, \rho_i) \in [s, s+q], \quad i = 1, \dots, M\}, \quad (5)$$

where L is the distance, M is the number of the prepared estimated images ($M=10,000$), $s=0, 0.001, \dots, 0.080$, and $q=0.001$. Also, A_τ is defined in the same way. The cardinality of A_ρ denotes the frequency of the quantized value q to each distance. Figure 4(a) presents a histogram with a quantized interval $[s, s+q]$ and A_ρ for $s=0, 0.001, \dots, 0.080$. The case of A_τ is shown in Fig. 4(b). A_ρ and A_τ each bears a strong resemblance to the other. Both estimated images (ρ_1, \dots, ρ_M) and (τ_1, \dots, τ_M) form a unimodal distribution. They are distant from the original points of average images $\bar{\rho}$ and $\bar{\tau}$. That is, their average images separate from the distribution of each estimated image. This shows that almost all the estimated images are distributed on thick spherical shells and their centers are the average images.

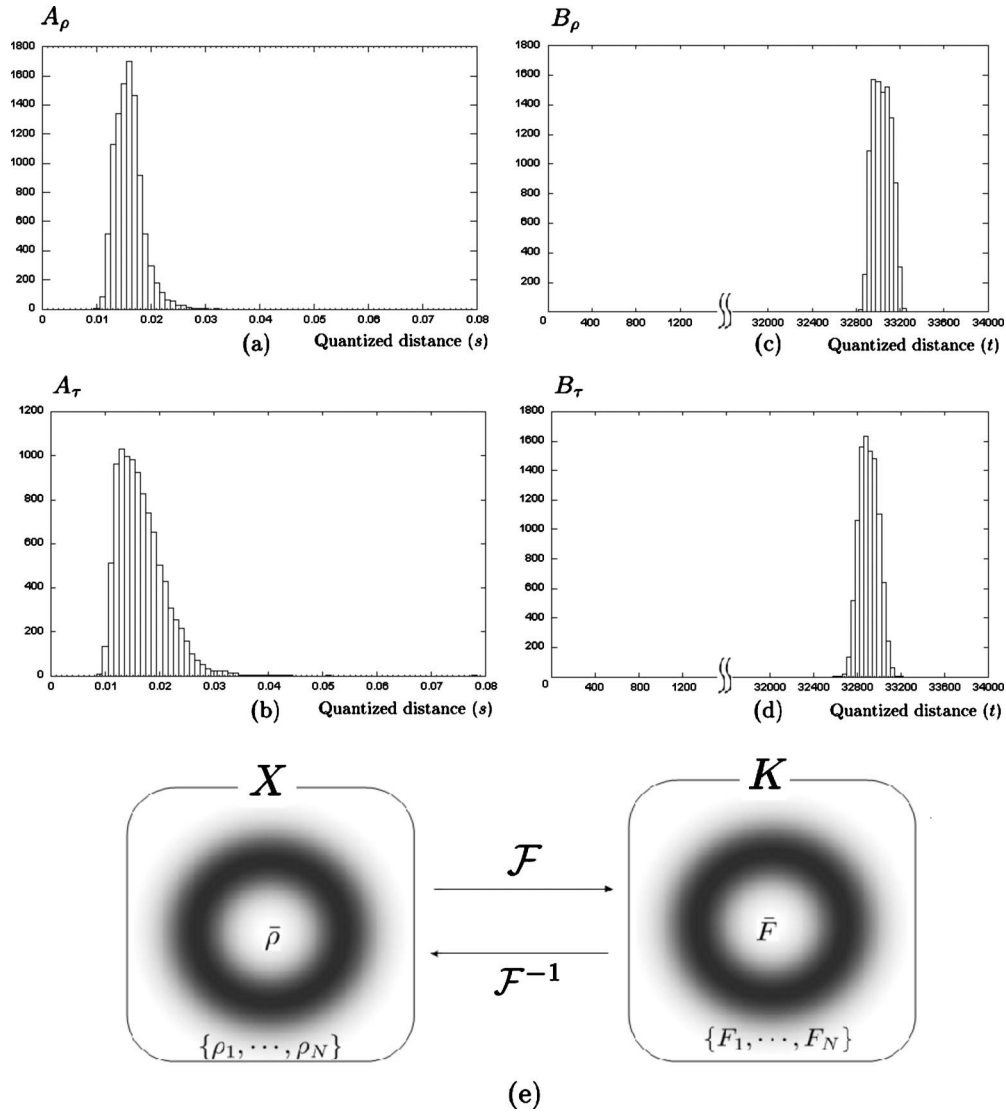


Fig. 4. (a) Histogram A_ρ of distance values between average image $\bar{\rho}$ and each estimated image ρ_j for $j=1, \dots, 10,000$. (b) Histogram A_τ of the distance value between the average image $\bar{\tau}$ and each estimated image τ_j for $j=1, \dots, 10,000$. (c) and (d) Histograms B_ρ and B_τ in the Fourier space that correspond to A_ρ and A_τ in the object space, respectively. (e) The relationship between the object and Fourier spaces X and K is schematically presented. Various distinct estimated images (ρ_j , with $j=1, \dots, N$) are distributed around the center $\bar{\rho}$, and their Fourier transformed functions [$F_j = \mathcal{F}(\rho_j)$, with $j=1, \dots, N$] are also distributed around the center \bar{F}_ρ . In the case of the estimated images $\{\tau_1, \dots, \tau_N\}$, the relationship between the two spaces is the same as in the case $\{\rho_1, \dots, \rho_N\}$.

Let us also investigate the structure of the Fourier transformation $F_{\rho_i} = \mathcal{F}(\rho_i)$ (for $i=1, \dots, M$) and the average $F_{\bar{\rho}} = \mathcal{F}(\bar{\rho})$. We note that averaging $\{\rho_1, \dots, \rho_M\}$ is equivalent to that of $\{F_{\rho_1}, \dots, F_{\rho_M}\}$ by using

$$\mathcal{F}\left(\frac{1}{M} \sum_{i=1}^M \rho_i\right) = \frac{1}{M} \sum_{i=1}^M \mathcal{F}(\rho_i) = \frac{1}{M} \sum_{i=1}^M F_{\rho_i}. \quad (6)$$

We define the subsets of $\{F_{\rho_1}, \dots, F_{\rho_M}\}$ that satisfy the constraint of the distance from $F_{\bar{\rho}}$ to each F_{ρ_i} as

$$B_\rho = \{F_{\rho_i} | L(F_{\bar{\rho}}, F_{\rho_i}) \in [t, t+q'), \quad i=1, \dots, M\}, \quad (7)$$

where $t=0, 40, \dots, 34,000$ and $q'=40$. In the same way, B_τ is defined using $F_{\tau_i} = \mathcal{F}(\tau_i)$ ($i=1, \dots, M$) and average $F_{\bar{\tau}} = \mathcal{F}(\bar{\tau})$. The cardinalities of B_ρ and B_τ are presented in Figs. 4(c) and 4(d), respectively. They form a unimodal distribution. $\{F_{\rho_1}, \dots, F_{\rho_M}\}$ and $\{F_{\tau_1}, \dots, F_{\tau_M}\}$ are away

from the averages $F_{\bar{\rho}}$ and $F_{\bar{\tau}}$ of the original points in the graphs, respectively. That is, their averages are separated from the Fourier transformation of the estimated images. This shows that almost all these transformations are distributed on thick spherical shells and that the centers are the averages. Thus, these are also distributed in the spherical shell structure in the Fourier space. The histograms of B_ρ and B_τ resemble each other. Figure 4(e) schematically shows the spherical shell structures in both spaces.

4. DISCUSSION

Noise in the observation of Fourier intensity is an obstacle to finding a plausible Fourier phase. In the case of Fourier intensity contaminated by Poisson noise, a spherical shell structure of the distribution consisting of

phase-retrieved images is found in the object space through numerical simulations. This indicates the effectiveness of using the average of many different phase-retrieved images obtained by experimental diffraction waves [18–20]. We performed many simulations using different images from Fig. 2(a); however, all these simulations revealed a spherical shell structure. Another interesting feature was found in the ensemble of retrieved images. The phase-retrieved images were not distributed uniformly and were not dense. They formed a fractal-like arrangement. Iterative Fourier transform is a statistical dynamical system. The spherical shell structure might be an attractive fractal-like invariant set that is in the final state of iterations. The center of the averaging image also might be a singular point as a repeller. This is related to dynamical systems based on the iterated projections by Elser [21]. This paper is, to the best of our knowledge, the first step toward an advanced analysis based on the structure of the distribution of phase-retrieved images. The investigation of the averaging methods using recent experimental results [22,23] of our groups in electron microscopy is also one of the prominent future related works. The more precise characteristics of the structure and the spatial resolution of the final image by the averaging methods remain to be elucidated.

ACKNOWLEDGMENTS

We would like to thank the reviewers for the constructive comments and suggestions.

REFERENCES

1. D. Sayre, "Some implications of a theorem due to Shannon," *Acta Crystallogr.* **5**, 843 (1952).
2. R. W. Gerchberg and W. O. Saxton, "A practical algorithm for the determination of phase from image and diffraction plane pictures," *Optik (Stuttgart)* **35**, 237–246 (1972).
3. J. R. Fienup, "Phase retrieval algorithms: a comparison," *Appl. Opt.* **21**, 2758–2769 (1982).
4. J. Miao, D. Sayre, and H. N. Chapman, "Phase retrieval from the magnitude of the Fourier transforms of nonperiodic objects," *J. Opt. Soc. Am. A* **15**, 1662–1669 (1998).
5. J. Miao, P. Charalambous, J. Kirz, and D. Sayre, "Extending the methodology of X-ray crystallography to allow imaging of micrometer-sized non-crystalline specimens," *Nature* **400**, 342–344 (1999).
6. J. C. H. Spence, in *Science of Microscopy*, P. W. Hawkes and J. C. H. Spence, eds. (Springer, 2007).
7. J. Miao, T. Ishikawa, B. Johnson, E. H. Anderson, B. Lai, and K. O. Hodgson, "High resolution 3D x-ray diffraction microscopy," *Phys. Rev. Lett.* **89**, 088303 (2002).
8. J. Miao, T. Ishikawa, E. H. Anderson, and K. O. Hodgson, "Phase retrieval of diffraction patterns from noncrystalline samples using the oversampling method," *Phys. Rev. B* **67**, 174104 (2003).
9. Y. Nishino, J. Miao, and T. Ishikawa, "Image reconstruction of nanostructured nonperiodic objects only from oversampled hard x-ray diffraction intensities," *Phys. Rev. B* **68**, 220101(R) (2003).
10. H. N. Chapman, A. Barty, M. J. Bogan, S. Boutet, M. Frank, S. P. Hau-Riege, S. Marchesini, B. W. Woods, S. Bajt, W. H. Benner, R. A. London, E. Plönjes, M. Kuhlmann, R. Treusch, S. Düsterer, T. Tschentscher, J. R. Schneider, E. Spiller, T. Möller, C. Bostedt, M. Hoener, D. A. Shapiro, K. O. Hodgson, D. van der Spoel, F. Burmeister, M. Bergh, C. Caleman, G. Huldt, M. M. Seibert, F. R. N. C. Maia, R. W. Lee, A. Szöke, N. Timneanu, and J. Hajdu, "Femtosecond diffractive imaging with a soft-x-ray free-electron laser," *Nat. Phys.* **2**, 839–843 (2006).
11. J. M. Zuo, I. Vartanyants, M. Gao, R. Zhang, and L. A. Nagahara, "Atomic resolution imaging of a carbon nanotube from diffraction intensities," *Science* **300**, 1419–1421 (2003).
12. U. Weierstall, Q. Chen, J. C. H. Spence, M. R. Howells, M. Isaacson, and R. R. Panepucci, "Image reconstruction from electron and X-ray diffraction patterns using iterative algorithms: experiment and simulation," *Ultramicroscopy* **90**, 171–195 (2002).
13. O. Kamimura, K. Kawahara, T. Doi, T. Dobashi, T. Abe, and K. Gohara, "Diffraction microscopy using 20 kV electron beam for multiwall carbon nanotubes," *Appl. Phys. Lett.* **92**, 024106 (2008).
14. S. Morishita, J. Yamasaki, K. Nakamura, T. Kato, and N. Tanaka, "Diffractive imaging of the dumbbell structure in silicon by spherical-aberration-corrected electron diffraction," *Appl. Phys. Lett.* **93**, 183103 (2008).
15. R. L. Sandberg, A. Paul, D. A. Raymondson, S. Hädrich, D. M. Gaudiosi, J. Holtsnider, R. I. Tobey, O. Cohen, M. M. Murnane, H. C. Kapteyn, C. Song, J. Miao, Y. Liu, and F. Salmassi, "Lensless diffractive imaging using tabletop coherent high-harmonic soft-x-ray beams," *Phys. Rev. Lett.* **99**, 098103 (2007).
16. G. Oszlányi and A. Suto, "Ab initio structure solution by charge flipping," *Acta Crystallogr.* **A60**, 134–141 (2004).
17. K. Choi and A. Lanterman, "Phase retrieval from noisy data based on minimization of penalized I -divergence," *J. Opt. Soc. Am. A* **24**, 34–49 (2007).
18. J. Miao, Y. Nishino, Y. Kohmura, B. Johnson, C. Song, S. H. Risbud, and T. Ishikawa, "Quantitative image reconstruction of GaN quantum dots from oversampled diffraction intensities alone," *Phys. Rev. Lett.* **95**, 085503 (2005).
19. H. N. Chapman, A. Barty, S. Marchesini, A. Noy, C. Cui, M. R. Howells, R. Rosen, H. He, J. C. H. Spence, U. Weierstall, T. Beetz, C. Jacobson, and D. Shapiro, "High-resolution ab initio three-dimensional x-ray diffraction microscopy," *J. Opt. Soc. Am. A* **23**, 1179–1200 (2006).
20. P. Thibault, V. Elser, C. Jacobsen, D. Shapiro, and D. Sayre, "Reconstruction of a yeast cell from X-ray diffraction data," *Acta Crystallogr.* **A62**, 248–261 (2006).
21. V. Elser, "Phase retrieval by iterated projections," *J. Opt. Soc. Am. A* **20**, 40–55 (2003).
22. O. Kamimura, T. Dobashi, K. Kawahara, T. Abe, and K. Gohara, "10-kV diffractive imaging using newly developed electron diffraction microscope," *Ultramicroscopy* **110**, 130–133 (2010).
23. K. Kawahara, K. Gohara, Y. Maehara, T. Dobashi, and O. Kamimura, "Beam-divergence deconvolution for diffractive imaging," *Phys. Rev. B* **81**, 018404 (2010).